Supporting Information

Carbon encapsulated RuO_2 nano-dots anchoring on graphene as electrode for asymmetric supercapacitor with ultralong cycle life in ionic liquid electrolyte

Baoshou Shen,[ab] Xu Zhang,[a] Ruisheng Guo,[a] Junwei Lang,[a] Jiangtao Chen[a] and Xingbin Yan*[a]

[a] Laboratory of Clean Energy Chemistry and Materials, State Key Laboratory of Solid Lubrication, Lanzhou Institute of Chemical Physics, Chinese of Academy of Sciences, Lanzhou, 730000, P.R. China

[b] University of Chinese Academy of Sciences, Beijing, 100039, P.R. China.

* Corresponding author. Tel.: +86-931-4968055; fax: +86-931-4968055. E-mail address: xbyan@licp.cas.cn

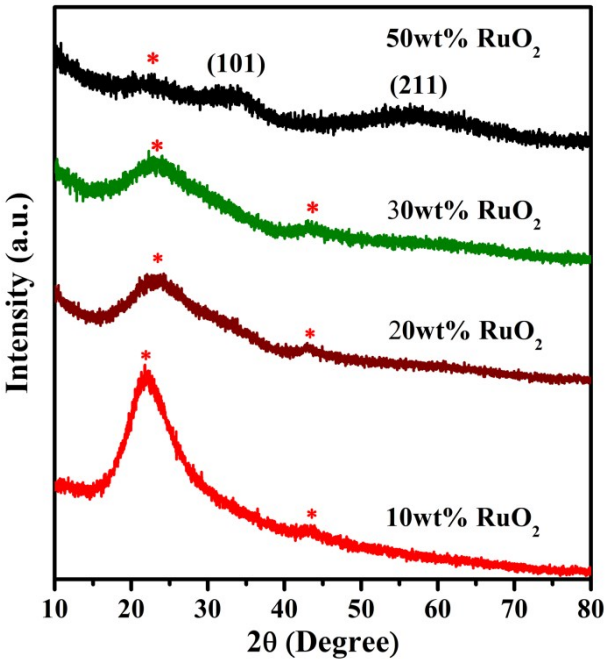

Figure S1. Powder XRD patterns of RuO_2/RGO composites with different loadings of RuO_2.

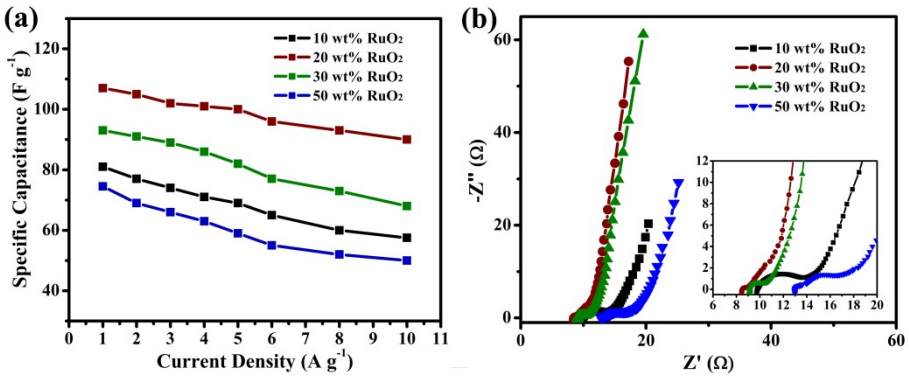

Figure S2. (a) The specific capacitances of RuO_2/RGO composites with different loadings of RuO_2 as a function of the discharge current density. (b) Corresponding Nyquist plots. Inset showing enlarged plots in high-frequency region.

As can be seen from Figure 2 and Figure S2, the specific capacitance of 10 wt% RuO_2/RGO composite electrode is about 81 F g^{-1}, which was between 93 F g^{-1} for the pure RGO electrode and 75 F g^{-1} for the pure RuO_2 electrode. Since a small amount of RuO_2 serving as spacers cannot be effectively prevent the agglomeration of RGO nanosheets, thus it didn't exhibit a positive synergistic effect between RGO and RuO_2 on improvement of the electrochemical performances of RuO_2/RGO composite, and 10 wt% RuO_2/RGO composite materials were similar to physical mixture of them. When the loadings of RuO_2 in the RuO_2/RGO composite reached up to 30 wt% or above 30 wt%, more and more RuO_2 nano-dots anchored on the RGO surface, this will greatly

increase the contact resistance between RGO and RuO_2, leading to the decrease of the electrochemical performances.

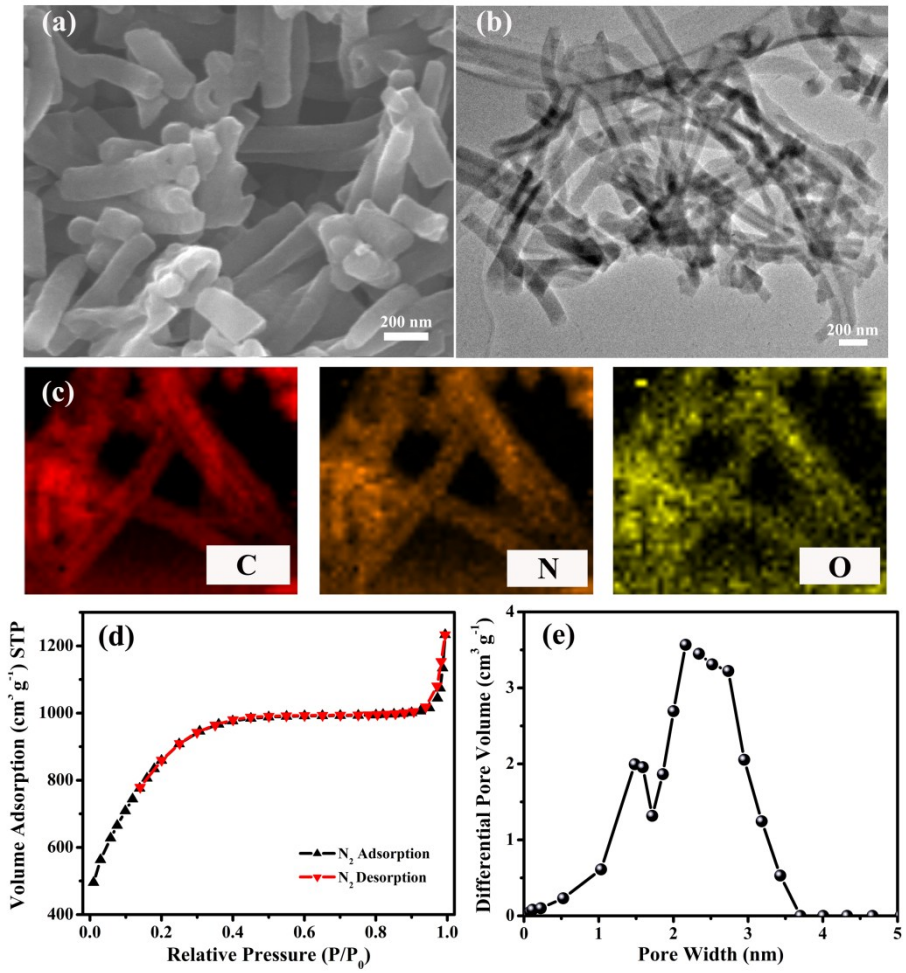

Figure S3. (a and b) SEM and TEM images of the APDC nanorods. (c) The element mappings of APDC corresponding to C, O and N. (d and e) The N_2 sorption isotherms and the corresponding pore size distribution of APDC nanorods.

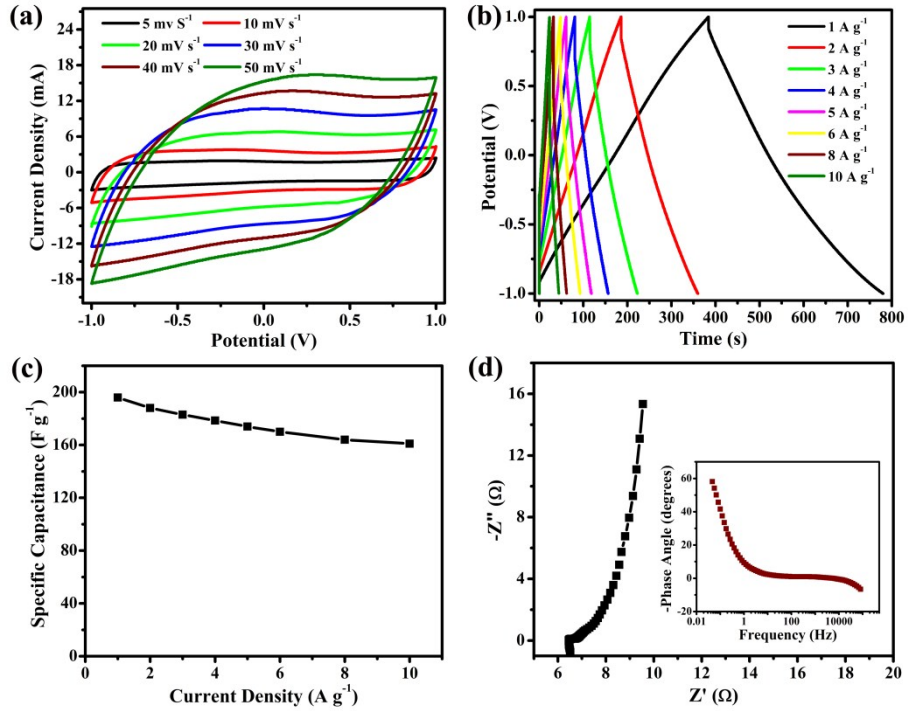

Figure S4. (a) CV curves of the APDC electrode at different scan rates. (b) GCD curves of the APDC electrode at different current densities. (c) The specific capacitance as a function of discharge current density. (d) The Nyquist plot of the APDC electrode, inset is plot of impedance phase angle versus frequency. The electrolyte is EMIM-BF_4 IL.

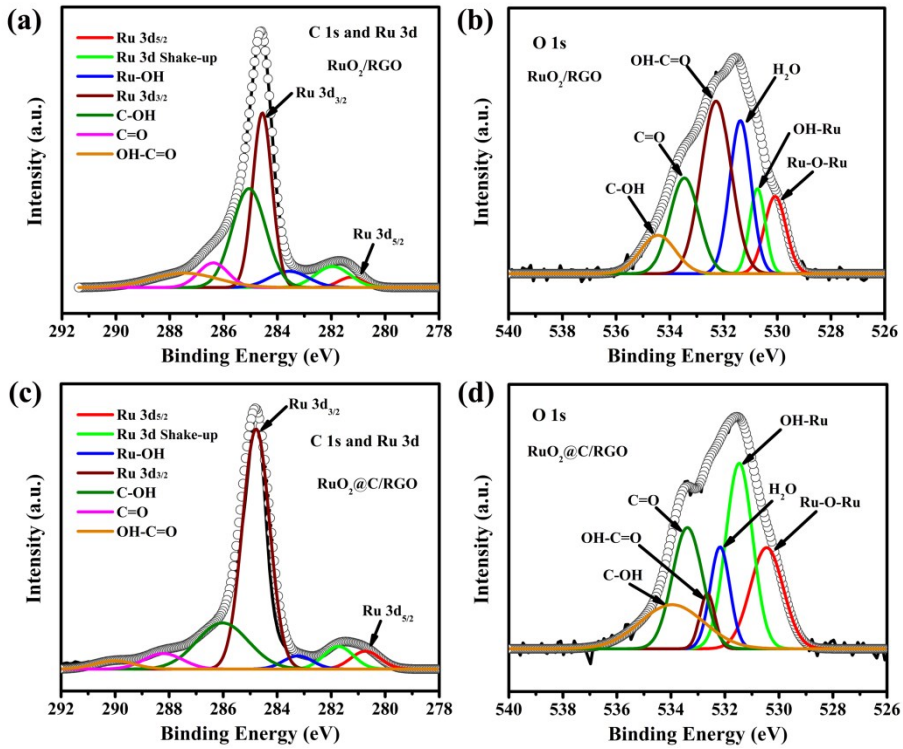

Figure S5. (a, b) Well-fitted XPS C 1s, Ru 3d and O 1s spectra of RuO_2/RGO. (c, d) Well-fitted XPS C 1s, Ru 3d and O 1s spectra of RuO_2@C/RGO (black solid lines are experimental data, the dark gray hollow lines are fitted results).

XPS characterization was performed to investigate the chemical state variation of the element in the RuO_2/RGO and RuO_2@C/RGO composite materials as shown in Figure S5. The XPS data in the C 1s region overlapped with Ru $3d_{3/2}$. Fortunately, the Ru $3d_{5/2}$ peak at about 281 eV corresponded to the binding energy of Ru^{4+}, suggesting the presence of RuO_2. The C 1s and Ru 3d were deconvoluted into seven components including the peaks assigned to the Ru 3d photoelectrons, at 281.0 eV (Ru $3d_{5/2}$ of RuO_2) and at 281.8 eV (a shake-up feature due to final state effects). The peak at 283.4 eV was attributed to RuOH. The peak at more than 285.0 eV came from C 1s of RGO.[1] Additionally, the well-fitted XPS O 1s also confirmed the existence of RuO_2 in the RuO_2/RGO and RuO_2@C/RGO composite materials, and oxygen-containing functional group were identified with HO-C=O (532.3 eV), C=O (533.5 eV) and C-OH (534.5 eV).[2] The relative content of the HO-C=O functional group decreased after carbon-encapsulated treatment, indicating the further reduction of RGO, which was conducive to improve the electrical conductivity and electrochemical stability of the RuO_2@C/RGO composite electrode.

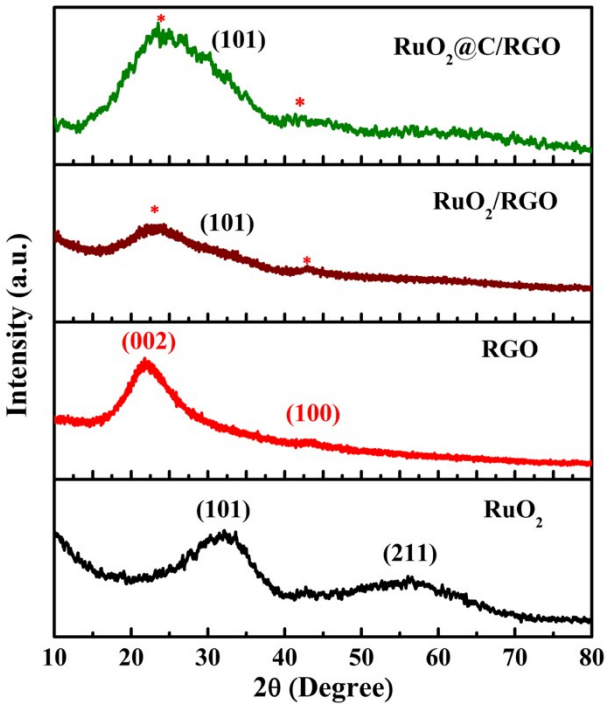

Figure S6. XRD patterns of RuO_2, RGO, RuO_2/RGO and RuO_2@C/RGO.

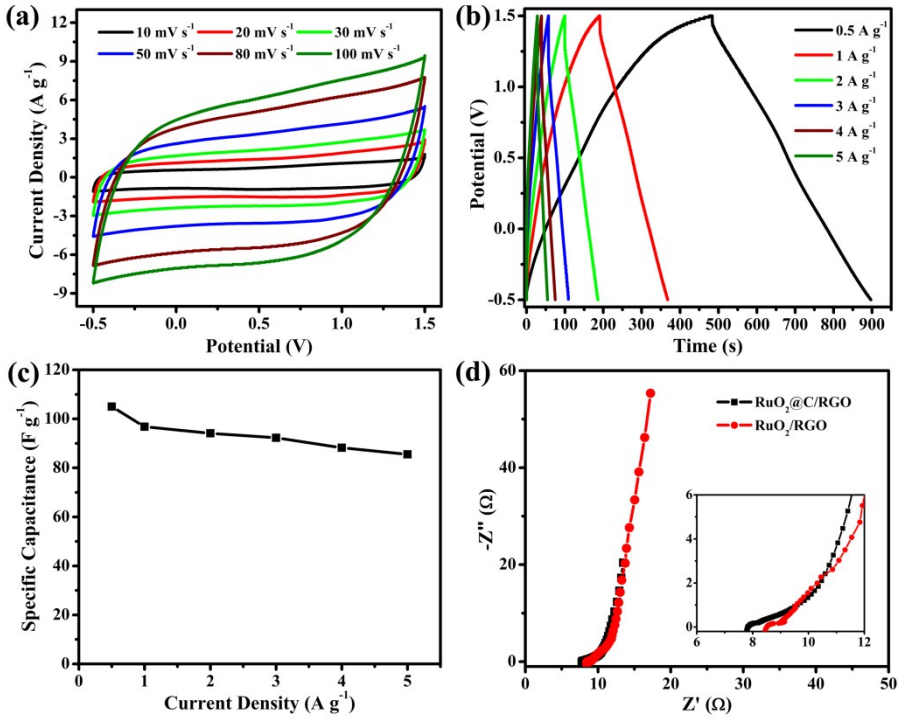

Figure S7. (a, b) CV and GCD curves of the RuO_2@C/RGO electrode under the annealing temperature of 400 ºC at different scan rates. (c) The corresponding specific capacitance as a function of the discharge current density. (d) The corresponding Nyquist plots of the RuO_2@C/RGO electrode. The electrolyte is EMIM-BF4 IL.

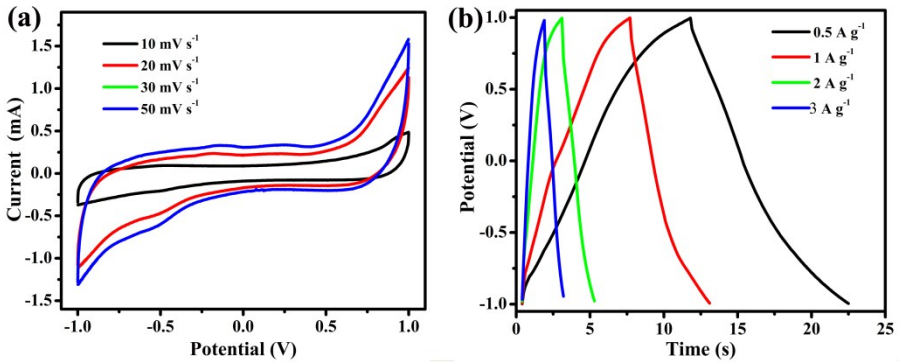

Figure S8. (a, b) CV and GCD curves of the amorphous carbon derived from the glucose according to the same process conditions prepared carbon-encapsulated RuO_2 to form RGO/RuO_2@C. The annealing temperature is 400 ºC. The electrolyte is EMIM-BF4 IL.

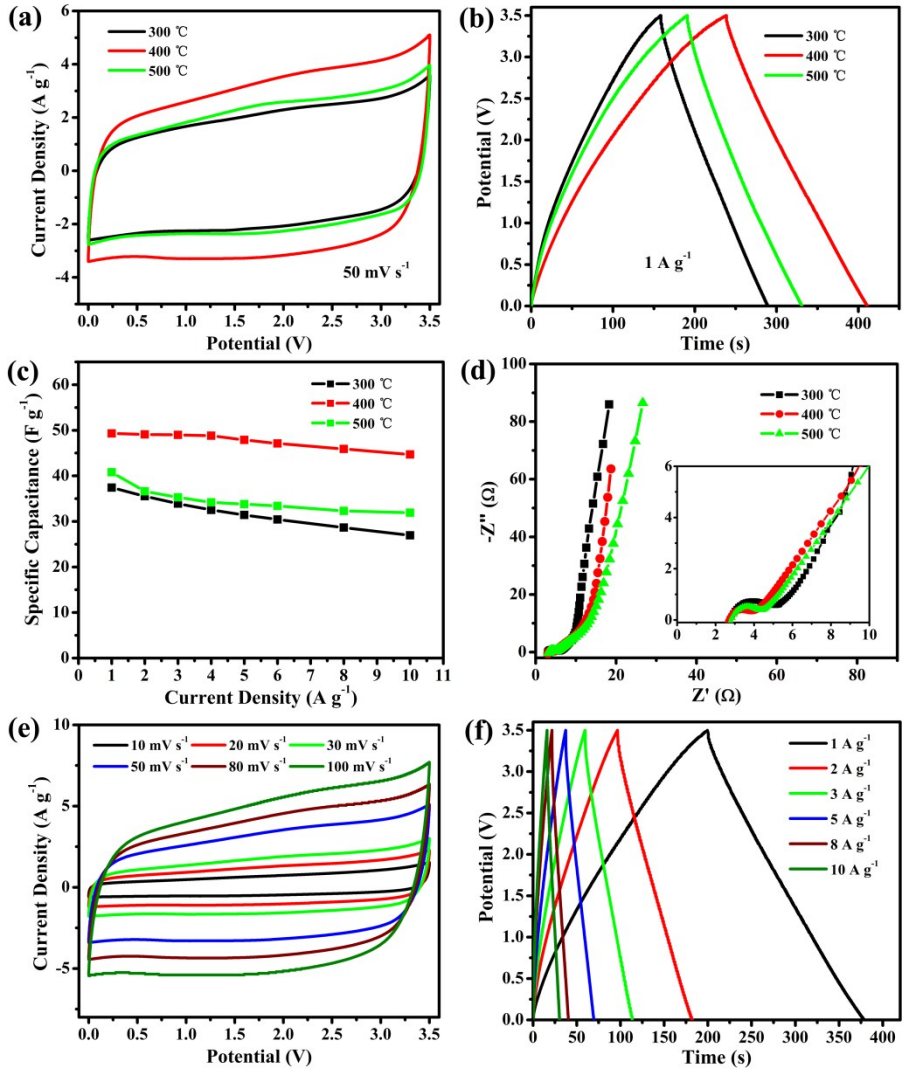

Figure S9. (a, b) CV and GCD curves of RuO_2@C/RGO//APDC asymmetric SCs at different annealing temperatures (300 ºC, 400 ºC and 500 ºC) when preparing the RuO_2@C/RGO electrode. (c) Comparison of the specific capacitances of the corresponding asymmetric SCs at different current densities. (d) The corresponding Nyquist plots of these asymmetric SCs. (e, f) CV and GCD curves of the RuO_2@C/RGO//APDC asymmetric SC at the annealing temperature of 400 ºC. The electrolyte is EMIM-BF_4 IL.

In order to obtain high-quality RuO_2@C/RGO electrode materials, we investigated the electrochemical properties of the RuO_2@C/RGO//APDC SCs at different annealing temperatures (300 ºC, 400 ºC and 500 ºC) when preparing the RuO_2@C/RGO electrode. The enclosed area of the CV curve at the annealing temperature of 400 ºC was found to be larger than that at 300 ºC and 500 ºC at the scan rate of 50 mV s^{-1}, suggesting a larger specific capacitance. The GCD curves also confirmed this. In addition, the RuO_2@C/RGO//APDC SC at 400 ºC have the largest specific capacitance, the smallest charge-transfer resistance (Rct=1.5 Ω) in IL electrolyte, as well as good

rate capability. The RuO_2@C/RGO//APDC SC at 300 ºC had the smallest specific capacitance and worst rate capability could be attributed to the low electrical conductivity of the RuO_2@C/RGO at a low annealing temperature. On the other hand, the oxygen-containing functional group could be decomposed or reduced on the surface of RGO at the high annealing temperature of 500 ºC, which wasn't beneficial to the diffusion of ion of IL electrolyte.

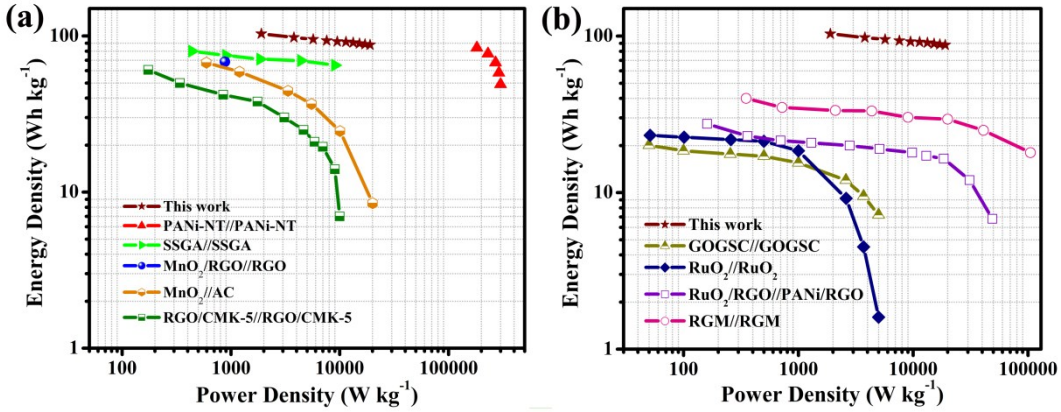

Figure S10. (a) The energy-power curve of the RuO_2@C/RGO//APDC asymmetric SC compared with values previously reported in the literatures using ILs as electrolyte. (b) Ragone plot related to energy densities and power densities of the RuO_2-containing SCs, including RuO_2 symmetric SC[8], hydrous RuO_2/RGO composite (GOGSC) symmetric SC[8], RuO_2/RGO//polyaniline (PANi)/RGO asymmetric SC[9], hydrous RuO_2 anchored graphene and CNT hybrid foam (RGM) symmetric SC[10].

As shown in the Ragone plots, The RuO_2@C/RGO//APDC asymmetric SC (ASC) could reach a maximum energy density of 103 Wh kg^{-1} at a low power density of 1.9 kW kg^{-1}, and it remains at 87.6 Wh kg^{-1} at a high power density of 19 kW kg^{-1}, indicating superior combination of high energy and power density. And such energy density value was substantially higher than that of reported IL-based SC devices, such as polyaniline nanotube (PANi-NT) symmetric SC (84 Wh kg^{-1}),[3] single-walled carbon nanotube spaced graphene aerogel (SSGA) symmetric SC (80 Wh kg^{-1}),[4] MnO_2/graphene//graphene (MnO_2/RGO//RGO) asymmetric SC (68.4 W h kg^{-1}),[5] MnO_2//activated carbon (MnO_2//AC) asymmetric SC (67.5 Wh kg^{-1})[6] and RGO+CMK-5 symmetric SC.[7]

When comparing our energy density and power density values with reported RuO_2-containing SC devices in aqueous electrolytes, our-assembled RuO_2@C/RGO//APDC SC had more obvious advantages in energy density and power density. And our energy density values

were substantially higher than that of reported RuO_2-containing SC devices, such as RuO_2 symmetric SC,[8] GOGSC symmetric SC,[8] RuO_2/RGO//PANi/RGO asymmetric SC[9] and RGM symmetric SC,[10] and the power densities were relatively high among the reported RuO_2-containing SCs.

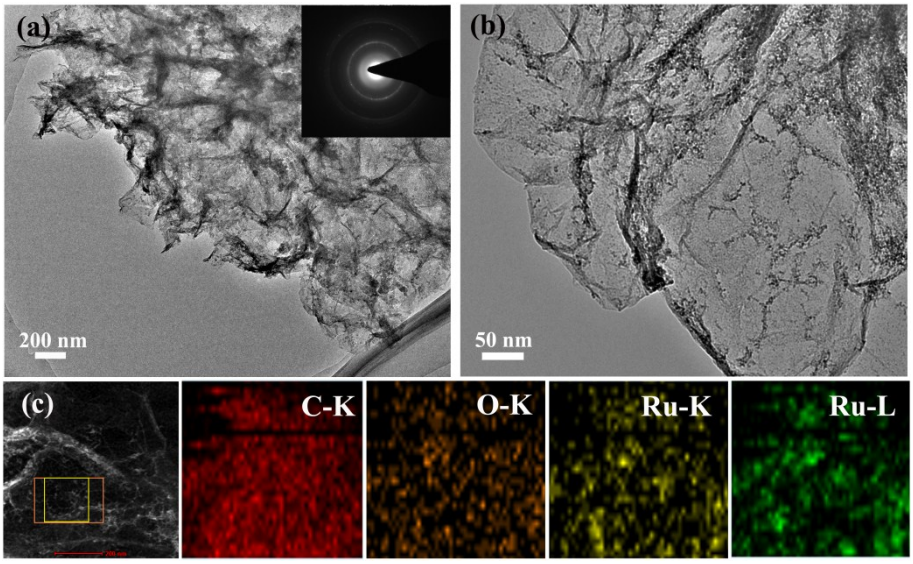

Figure 11. (a, b) TEM images of the RuO_2@C/RGO electrode material after 100 000 charge/discharge cycles. Inset is the SAED pattern. (c) TEM image and corresponding EDX mapping of C, O and Ru atoms after 100 000 charge/discharge cycles.

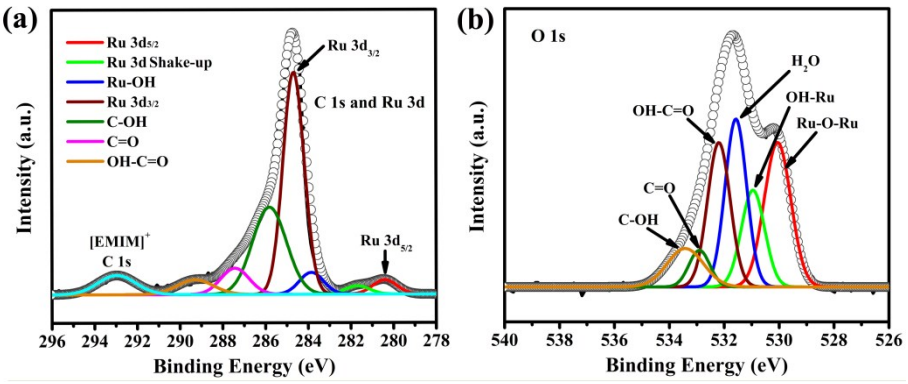

Figure S12. Well-fitted XPS C 1s, Ru 3d and O 1s spectra of the RuO_2@C/RGO electrode material after 100 000 charge/discharge cycles (black solid lines are experimental data, the dark gray hollow lines are fitted results).

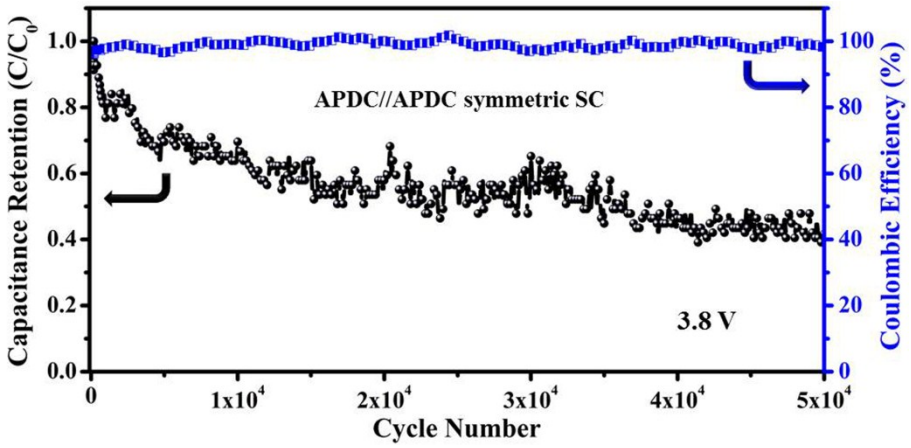

Figure S13. Cycling stability and coulombic efficiency of the APDC//APDC symmetric SC at the current density of 3 A g^{-1} for 50 000 cycles with the potential window of 3.8 V. The electrolyte is EMIM-BF_4 IL.

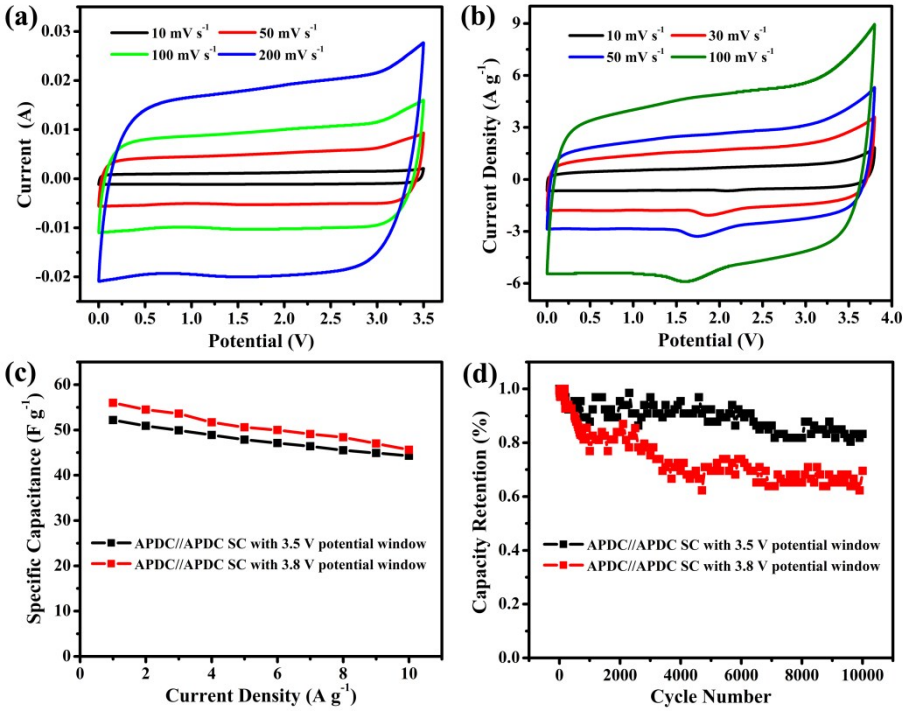

Figure S14. (a, b) CV curves of the APDC//APDC symmetric SC with the different potential windows of 3.5 V and 3.8 V, respectively. (c) Comparison of the specific capacitances of the APDC//APDC symmetric SC with the different potential windows of 3.5 V and 3.8 V, respectively. (d) The corresponding cycling stability of APDC//APDC symmetric SC with the different potential windows.

On the one hand, enlarging the potential window up to 3.8 V can enhance the specific capacitance, but the symmetry of CV curves got worse and the polarization phenomenon was more obvious according to the comparison results with the different potential windows of 3.5 V

and 3.8 V. Additionally, the rate capability could be slightly improved when the potential window was 3.5 V. During charge storage process, more ions of electrolyte will be facilitated to diffuse into the porosity with smaller pore size of APDC electrode materials under a greater polarization voltage (corresponding to a bigger potential window), which could contribute to a larger specific capacitance, but on the other hand, this could also make the ions of electrolyte in the micropores of APDC not completely desorb in the process of discharge, leading to more irreversibility of charge storage and a poor cycling stability as shown in Figure S13 and Figure S14d. In a word, the shallow discharge and charge with a smaller potential window could ensure a better reversibility, which would be beneficial to the cycling stability. While a larger potential window would result in more irreversibility and a poor cycling stability.

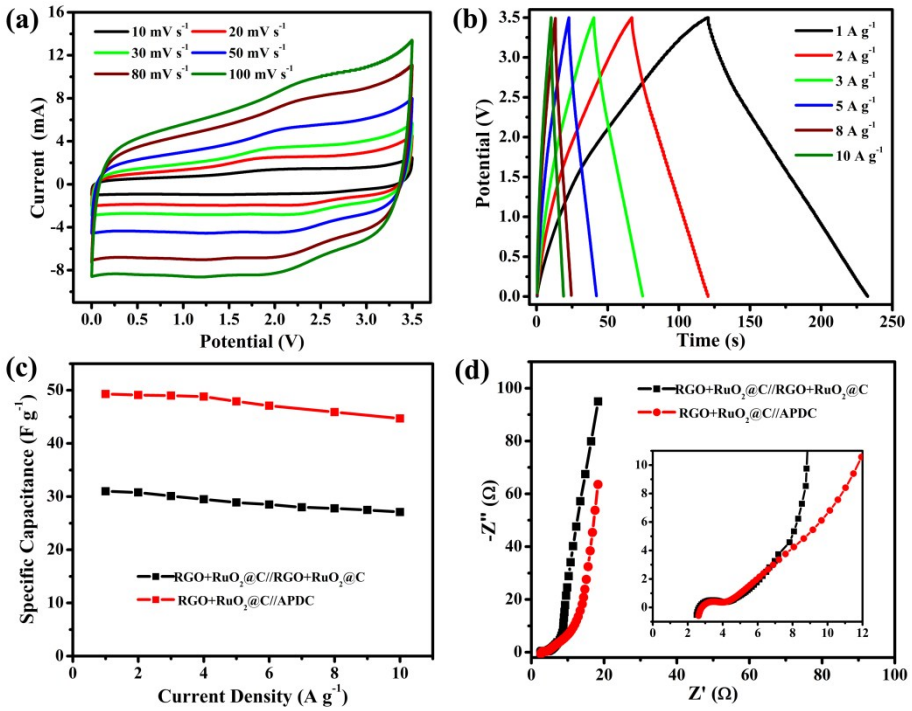

Figure S15. (a, b) CV and GCD curves of the RuO_2@C/RGO//RuO_2@C/RGO symmetric SC with the potential window of 3.5 V. (c) Comparison of the specific capacitances of the RuO_2@C/RGO//RuO_2@C/RGO symmetric SC and RuO_2@C/RGO//APDC asymmetric SC. (d) The corresponding Nyquist plots of RuO_2@C/RGO//RuO_2@C/RGO and RuO_2@C/RGO//APDC, respectively.

The CV curves of the RuO_2@C/RGO//RuO_2@C/RGO symmetric SC could maintained a nearly rectangular shape ranging from 10 mV s^{-1} to 100 mV s^{-1}, indicating fast charging and discharging capability and a good capacitive behavior. However, the CV curves began to appear

the polarization phenomenon with the increase of scan rate. It was probably because of relatively larger potential window for the symmetric SC. The GCD curves presented a good reversibility of charge storage and small voltage drop. As can be seen from Figure S15c, the specific capacitance (31.5 F g^{-1}) of RuO_2@C/RGO//RuO_2@C/RGO SC at the current density of 1 A g^{-1} retained about 86 % (27.1 F g^{-1}) when the current density was up to 10 A g^{-1}, suggesting a better rate capability. In addition, the RuO_2@C/RGO//RuO_2@C/RGO SC exhibited a little smaller equivalent series resistance and better diffusion capability than RuO_2@C/RGO//APDC SC, but had a smaller specific capacitance. In a word, our-assembled RuO_2@C/RGO//APDC asymmetric SC enhanced the specific capacitance relative to the RuO_2@C/RGO//RuO_2@C/RGO symmetric SC, and significantly improved the cycling stability relative to the APDC//APDC symmetric SC.

References

1 W. Wang, S. Guo, I. Lee, K. Ahmed, J. Zhong, Z. Favors, F. Zaera, M. Ozkan and C. S. Ozkan, *Sci. Rep.*, 2014, **4**, 4452.

2 Y. Wang, Y. Shao, D. W. Matson, J. Li and Y. Lin, *ACS Nano*, 2010, **4**, 1790-1798.

3 W. Chen, R. B. Rakhi and H. N. Alshareef, *J. Mater. Chem. A*, 2013, **1**, 3315-3324.

4 Q. Shao, J. Tang, Y. Lin, J. Li, F. Qin, J. Yuan and L.-C. Qin, *J. Power Sources*, 2015, **278**, 751-759.

5 X. Zhu, P. Zhang, S. Xu, X. Yan and Q. Xue, *ACS Appl. Mater. Interfaces*, 2014, **6**, 11665-11674.

6 X. Zhang, D. Zhao, Y. Zhao, P. Tang, Y. Shen, C. Xu, H. Li and Y. Xiao, *J. Mater. Chem. A*, 2013, **1**, 3706-3712.

7 Z. Lei, Z. Liu, H. Wang, X. Sun, L. Lu and X. S. Zhao, *J. Mater. Chem. A*, 2013, **1**, 2313-2321.

8 Z. S. Wu, D. W. Wang, W. Ren, J. Zhao, G. Zhou, F. Li and H. M. Cheng, *Adv. Funct. Mater.*, 2010, **20**, 3595-3602.

9 J. Zhang, J. Jiang, H. Li and X. S. Zhao, *Energy Environ. Sci.*, 2011, **4**, 4009–4015.

10 W. Wang, S. Guo, I. Lee, K. Ahmed, J. Zhong, Z. Favors, F. Zaera, M. Ozkan and C. S. Ozkan, *Sci. Rep.*, 2014, **4**, 4452.